Journal of Solid State Electrochemistry (2018) 22:1697–1710
https://doi.org/10.1007/s10008-017-3862-2

ORIGINAL PAPER

$La_{0.1}Ca_{0.9}MnO_3/Co_3O_4$ for oxygen reduction and evolution reactions (ORER) in alkaline electrolyte

Alagar Raj Paulraj [1] · Yohannes Kiros [1]

Received: 4 September 2017 / Revised: 5 December 2017 / Accepted: 9 December 2017 / Published online: 10 January 2018

Abstract

Non-precious metal bifunctional catalysts are of great interest for metal–air batteries, electrolysis, and regenerative fuel cell systems due to their performance and cost benefits compared to the Pt group metals (PGM). In this work, metal oxides of $La_{0.1}Ca_{0.9}MnO_3$ and nano Co_3O_{47} catalyst as bifunctional catalysts were used in oxygen reduction and evolution reactions (ORER). The catalysts were characterized by X-ray diffraction (XRD), scanning electron microscopy (SEM), transmission electron microscopy (TEM), and N_2 adsorption isotherms. The electrocatalytic activity of the perovskite-type $La_{0.1}Ca_{0.9}MnO_3$ and Co_3O_4 catalysts both as single and mixtures of both were assessed in alkaline solutions at room temperature. Electrocatalyst activity, stability, and electrode kinetics were studied using cyclic voltammetry (CV) and rotating disk electrode (RDE). This study shows that the bifunctional performance of the mixed $La_{0.1}Ca_{0.9}MnO_3$ and nano Co_3O_4 was superior in comparison to either $La_{0.1}Ca_{0.9}MnO_3$ or nano Co_3O_4 alone for ORER. The improved activity is due to the synergistic effect between the $La_{0.1}Ca_{0.9}MnO_3$ and nano Co_3O_4 structural and surface properties. This work illustrates that hybridization between these two metal oxides results in the excellent bifunctional oxygen redox activity, stability, and cyclability, leading to a cost-effective application in energy conversion and storage, albeit to the cost of higher catalyst loadings.

Keywords Alkali electrolyte · Bifunctional electrocatalyst · Oxygen reduction · Oxygen evolution · Perovskite/spinel catalyst

Introduction

Energy security and climate change are widely discussed due to the depletion of fossil fuels and adverse emissions produced while utilizing them. Currently, the energy demand and CO_2 emission are 18 TW and 32 Gt year^{-1}, respectively, and are predicted to reach 26 TW and 44 (55 total greenhouse gases (GHG)) Gt year^{-1} at 2040 [1, 2]. The GHG emissions are considered to be major contributors to the anthropogenic climate change. Ambitious targets were set by the recently signed Paris agreement (COP 21) to reduce global average temperature well below the 2 °C of preindustrial level in the twenty-first century [3]. To achieve this target, further emission levels should be reduced and restricted to 40 Gt year^{-1} of GHG by 2030 [4]. European Union has also set its own climate action plan for 80–95% reduction of GHG compared to the 1990 level. The EU has chosen the following sustainable means to meet the target: energy efficiency, renewable energy, nuclear energy, and carbon capture and storage (CCS). In particular, the renewable energy's contribution to the total energy consumption is projected to increase from the current 10 to 50% by 2050 according to the high renewables scenario [5]. The major important renewable energy sources are wind and solar and are projected to reach 26 and 11% of the total energy demand by 2050 [6, 7]. These two systems are intermittent and very much dependent on weather conditions. Therefore, their seamless integration into the grid for transmission to the end user requires a large-scale energy storage system. Currently, we are only able to store 1% of the total energy produced, and 98% of it accounts to gravitational energy stored through pumped water in hydroelectric plants. These are situated in high and low elevations, which in turn affect the social life and ecology of the sites [8]. Electrochemical energy storage systems have attractive features such as modularity,

---

Electronic supplementary material The online version of this article (https://doi.org/10.1007/s10008-017-3862-2) contains supplementary material, which is available to authorized users.

✉ Alagar Raj Paulraj
arpau@kth.se

[1] Department of Chemical Engineering, KTH Royal Institute of Technology, SE-100 44 Stockholm, Sweden

scalability, fast response time, and high-energy efficiency, while they offer a wide range of energy and power densities, charge, discharge and life cycle, and capital cost [9].

Iron–air and Zn–air batteries in their early applications delivered energy densities up to 80 and 200 Wh kg^{-1} [10, 11]. The available iron and zinc reserves are 100 and 0.150 billion tons, respectively [12]. They both use metals as negative electrodes and a bifunctional oxygen electrode as cathode. Oxygen redox reactions take place at the cathode which is the fundamental basis for a number of electrochemical systems such as metal–air batteries, fuel cells, and electrolyzers (water and chlor-alkali) [13–16]. Even though the theoretical capacities of Fe and Zn electrodes, respectively, are 764 and 1080 mAh g^{-1}, the capacities of the full cell comprising them are limited by the cathodic reactions at the positive electrode. Significant voltage losses arise during the charge and discharge reactions at the bifunctional air electrode due to the sluggish kinetics leading to significant overvoltages. In alkaline media, the oxygen reduction proceeds by two reaction pathways: (1) the direct 4e^{-} and (2) the peroxide-mediated successive 2e^{-}, followed by reduction and disproportionation or decomposition of the peroxide [17]. The peroxide pathway is not desirable due to the corrosive species that affect the electrode materials and the active transition metal ions [18].

Some group of metals favor the direct 4e^{-} pathway such as Pt group, pyrocholre, and perovskite families, whereas peroxide path is favored by carbon materials, Hg, Au, and most of the transition metals and oxides [18, 19]. The platinum group metals (PGM) such as Pt, RuO_2, and IrO_2 are regarded as state-of-the-art electrocatalysts for both the oxygen reduction reaction (ORR) and oxygen evolution reaction (OER) [20–24]. Although very low amount of PGM are currently incorporated in the electrode composites, they possess poor stability and their high cost due to limited availability hinders large-scale application and commercialization.

Perovskites with ABO_3 structure have been considered as promising candidate electrocatalysts for the cathode, due to their bifunctionality, cost, availability, and stable performances in aqueous alkaline electrolytes. In ABO_3, generally A belongs to rare-earth divalent ion (such as La, Ce, Nd, Sm, Gd, Dy, Yd, Ho, and Y) and alkaline earth elements (Ca and Sr) while B is a transition metal (Cr, Mn, Fe, Co, Ni, Cu). La-based perovskites outperform other A site elements due to it is high ionic size [25]. Various perovskites have been developed such as $LaCrO_3$, $LaNiO_3$, $LaMnO_3$, $LaFeO_3$, and $LaCoO_3$ [15, 19, 26]. Among them, Mn and Co-based perovskites have shown stable and high oxygen reduction and evolution reaction (ORER) performance due to their oxidation state and spin configuration. Bifunctional ORER performance of the perovskites follow a volcano-type curve, based on the occupancy of e_g electronic state as primary activity descriptor, and electronegativity and spin state are considered as a secondary activity descriptor. e_g electron occupancy < 1 is favored for ORR, and for OER, it should be $e_g > 1$ [27–29]. Manganite-based perovskite's oxidation state and e_g electron filling vary from less than one to more than one based on A site and B site substitution. Altering the A and B sites results in interesting properties such as oxide ion mobility, electronic conductivity, and oxygen vacancies, which in turn augment the electrocatalytic properties on scale with or even better than PMG [30, 31]. Alkaline earth groups have similar ionic radii to lanthanides, are stable in high-temperature synthesis, and are low cost. Therefore, they are usually more or less substituted in place of the lanthanides. A site substitution results in increased current density and surface oxygen vacancies, conductivity, and stable crystal structure [15]. B site cations affect the bond forming ability of B to oxygenated compounds. Several combinations of perovskite with Mn in the B site were studied such as $La_{1-x}Ca_xMnO_3$, $CaMnO_3$, and $Ca_2Mn_2O_5$ [32]. Their surface oxygen vacancies provide additional active sites for the oxygen redox activity. $Ca_2Mn_2O_5$ ($e_g \approx 1$) has shown to have high OER performance, thanks to its molecular porosity and distorted structure [33]. As mentioned above, Ca substitution results in mixed valence state of Mn ($e_g < 1$), which consecutively produces oxygen vacancies by charge compensation and could promote the charge transfer and peroxide reduction [34]. $La_{1-x}Ca_xMnO_3$ has shown high conductivity and better bifunctional performance at even high porosity [35, 36]. In non-stoichiometric $La_{0.1}Ca_{0.9}MnO_3$, Ca substitution results in increased amount of Mn^{4+} concentration, which in turn provides high conductivity and enhances the discharge performance comparable to MnO_2 [16, 37, 38]. Though it has high ORR performance, its oxygen evolution performance has shown limitations.

Spinel Co_3O_4 is a low-cost magnetic p-type semiconductor with good structural stability and low environmental foot print and is commonly used in Li-ion battery, supercapacitor, solid-state sensors, heterogeneous catalyst, pigment, optical devices, photocatalyst, and oxygen evolution electrocatalyst [39, 40]. In recent years, there have been several studies reporting high OER activity with stable bifunctional performance of Co_3O_4 due to its mixed valance states [5, 41–45]. Although pure spinel itself is an efficient OER catalyst, its ORR performance is limited due to low conductivity and surface interaction. Recently, numerous strategies with complex or simple processes have been used for the preparation of Co_3O_4 showing substantial differences in size, shape, and surface properties for various applications [40, 45–50]. There have been different co-catalysts mixed with Co_3O_4 to achieve high and stable bifunctional activity [44, 48, 51–53]. Partial substitution of the spinel Co_3O_4 tetrahedral sites with Ni, Mn, Cu, or Zn has resulted in improved performance, where the electronegativity of the dopant in the M–O bond tunes the catalytic properties. The electronegativity difference between Mn (1.55) and Co (1.80) is suggested to play important role in electron withdrawal and accepting properties [14, 54–57].

More research effort has been centered on manganese and cobalt-based bifunctional catalysts, either alone or in mixture with other metals, due to their performance and abundance. MnO_2–perovskite mixed catalysts have shown to perform well for bifunctional applications in alkaline electrolyte [58].

In this work, we prepared nanostructured Co_3O_4 through facile synthesis method at low temperatures by precipitation and aqueous phase oxidation and high surface area $La_{0.1}Ca_{0.9}MnO_3$ through precipitation reaction, calcination, and followed at instant quenching. The oxide nanoparticles prepared with phase purity were characterized by XRD, SEM, TEM, and N_2 adsorption isotherm. The electrochemical properties of the $La_{0.1}Ca_{0.9}MnO_3$ and nano Co_3O_4 were investigated for their bifunctional activity and kinetics by cyclic voltammetry (CV) and linear sweep voltammetry (LSV) coupled with RDE. Single oxides as well as the combinations of the mixed oxides were for the first time studied for their OE and OR in order to evaluate their synergistic relationship for respective reactions and their stability in alkaline solutions.

Experimental

Preparation of $La_{0.1}Ca_{0.9}MnO_3$

All of the chemical reagents used for the preparation of the catalysts were of analytical grade and were applied without further purification. The perovskite $La_{0.1}Ca_{0.9}MnO_3$ (LCMO) was prepared by the precipitation method using sodium carbonate as supporting electrolyte. The precursors of alkaline earth, rare earth, and transitional metals such as Ca, La, and Mn were all in hydrated forms of nitrates (VWR Chemicals) and were dissolved in distilled water in a molar ratio of 1:0.11:0.9 of respective salt and heated separately at 60 °C. Sodium carbonate solution (0.5 M) heated at 60 °C was slowly added to the aforementioned mixture kept in a bigger container, which was then stirred vigorously to ensue reaction by precipitation. After several steps of washing and decanting the supernatant, the precipitate was filtered off and dried at 120 °C for 12 h. The dry sample was then homogenized in a high-speed mixer and heat-treated at 700 °C in air for 6 h and was subjected to instant quenching in a water-cooled zone. The powder was then filtered and washed with deionized water followed by 5% acetic acid in order to remove any unreacted metal species and reduce its strong alkalinity. This step was again followed by drying and pulverization as a final step for the procurement of the catalyst.

Preparation of Co_3O_4

Cobalt acetate tetra hydrate (9.66 g; VWR Chemicals) was dissolved in 200 ml of methanol (≥99.8%, Sigma-Aldrich) in a two-necked 0.5-l flat-bottom flask and heated below 65 °C on a hot plate with magnetic stirrer. A 1:1 mixture of deionized water and isopropyl alcohol in a total volume of 0.2 l volume was added, and the temperature was raised to 90 °C. During this vigorous mixing, a reflux condenser was connected on the top of the flask for cooling with tap water. As cobalt acetate got hydrolyzed into its constituent cation and anion, a solution of 1 M NaOH (100 ml) was then added dropwise to the above primary solution, where the pink solution was transformed to blue, green, and then brownish color upon sol-precipitation. Pure oxygen was bubbled at 50 ml min^{-1}, and the reaction continued for 16 h with a final black flocculent precipitate. This product was cooled to room temperature and settled for 1 day. The clear supernatant was then decanted and washed several times with ethanol and water mixtures, and the sediments were finally centrifuged at 3000 rpm. The nanoparticles were then dried in an oven at 60 °C overnight, heat-treated at 300 °C for removal of the solvents entrapped in the pore structure in N_2 atmosphere for 2 h and cooled, followed by grinding in a mixer to obtain the final product for continued characterization. The chemical reactions taking place during these steps are described below, where cobalt hydroxide precipitates with dissolution of the sodium salt (Eq. 1) in the aqueous phase and continuous formation of Co_3O_4 nanoparticles (Eq. 2) by the flow of oxygen.

$$\mathrm{Co(CH_3COO)_2} + 2NaOH \rightarrow \mathrm{Co(OH)_2(s)} + 2\ \mathrm{CH_3}COONa \tag{1}$$

$$3\ \mathrm{Co(OH)_2} + \S\ \mathrm{O_2} \rightarrow \mathrm{Co_3O_4(s)} + 3\mathrm{H2O} \tag{2}$$

Catalyst characterization

X-ray diffraction pattern was recorded by Siemens Diffractometer D5000, equipped with Ni-filtered Cu Kα radiation source ($\lambda = 0.154$ nm) at 40 kV and 30 mA in the 2θ range of 10°–80°. Phase identifications were done in EVA software, and corresponding powder diffraction file (PDF) numbers were reported. Scherrer's equation was used on the XRD patterns to calculate the crystallite size. Specific surface area, pore volume, and pore size distributions were obtained by the multipoint Brunauer–Emmet–Teller (BET) analyses and by Barret–Joyner–Halenda method (BJH), respectively, using N_2 adsorption isotherms (Micrometrics ASAP 2010) at a liquid N_2 temperature. Prior to the analyses, the samples were degassed at 250 °C for 4 h. Zeiss Ultra-55 SEM and JEOL JEM-2100F TEM were used to analyze the particle sizes and their morphologies.

Electrochemical characterization

The composite electrodes had a gas diffusion layer, current collector, and the electrode material in a series of arrangement.

They were prepared by mixing the electrode materials in the respective mass ratio (Table S1). The electrode composition was homogenized in a high-speed mixer at 6000 rpm (Waring® laboratory blender (LB20ES)) in the presence of hydrocarbon solvent (D-70® shellsol). After this, the filtered wet mass as active or catalyst layer was rolled on 100-mesh Ni wire screen on one side. The electrodes were pressed at 375 kg cm^{-2}. Following this step, the electrode was dried in an oven to remove the solvent at 100 °C. The other side of the electrode was brush-painted by a solution containing 20 wt% PTFE (60 wt% dispersion) and continued until a uniform sealed layer on the nickel mesh was achieved to maintain a proper gas diffusion layer for supply or evolution of oxygen. The electrodes were then sintered in N_2 atmosphere at 325 °C for 30 min [59]. The final electrode dimensions were 3 × 5 cm, thickness 0.35 ± 0.05 mm with an active material loading of 6.5–34 mg cm^{-2} (Table S1) depending on the type and composition of the catalyst. The ratios of the oxide catalysts to graphite and PTFE were maintained at 4–5:1:1, except for the 20 wt% Pt/C, which had a ratio of 4:1 to PTFE.

The rotating disk electrode (RDE) experiment was performed on glassy carbon (GC) electrode (0.196 cm^2). The RDE electrodes were prepared (Table S2) by ultrasonication (50 min) of the catalysts [LCMO, Co_3O_4, alone, or mixed together, 20 wt% Pt/C (ETEK) as a reference sample], graphite (Timrex HSAG 300, Timcal Ltd.), and 5 wt% Nafion as a binder having lower aliphatic alcohols and 3.6 g Milli-Q water with a resistivity of 18 MΩ and 0.4 g of isopropanol. The prepared ink 20 µl was drop-casted on the clean glassy carbon electrode and then dried.

The electrodes with bigger geometric area were tested in 6 M KOH (Sigma-Aldrich ACS reagent, ≥ 85%) in a three-electrode setup: composite electrode (working), Ni wire mesh (counter), and Hg/HgO (reference). The geometric area of 4 cm^2 with the catalyst layer was immersed in the electrolyte, while the diffusion layer at the rear side was exposed towards the oxygen flow. The ORER activity was measured using CV in the potential range of − 0.35 to 0.70 V vs. Hg/HgO at the scan rate of 5 mV s^{-1}.

In the RDE experiment, 1 M KOH as electrolyte prepared from Milli-Q water (18 MΩ cm) was used. Likewise, a three-electrode configuration was applied with the catalyst composite on the GC as a working electrode (see above), Pt ring mesh as counter electrode, and Hg/HgO in the same electrolyte as the reference electrode.

The RDE experiments for ORR were performed on LSV mode at scan rate of 2 mV s^{-1} with different rotation rates varying between 500 and 2500 rpm and in a potential range of 0.1 to − 0.9 V vs. Hg/HgO with constant oxygen-saturated solution. Prior to the RDE experiments, the catalysts were cycled at 10 mV s^{-1} scan rate in N_2 flow. The number of electrons involved in the reaction was obtained using the well-known Koutecky–Levich equation:

$$\frac{1}{j} = \frac{1}{j_k} + \frac{1}{j_d} = \frac{1}{j_k} + \frac{1}{B\omega^{1/2}} \tag{3}$$

where

$$B = 0.62nFC_O D_O^{2/3} \upsilon^{-1/6} \tag{4}$$

Here, j is the measured current density; j_k and j_d are the kinetic and diffusion limited current densities, respectively; ω is the rotation rate in rad s^{-1}; n is the number of electrons transferred in the reaction; F is the Faraday constant (96,487 C mol^{-1}); C_O is the oxygen bulk concentration in 1 M KOH (7.8×10^{-7} mol cm^{-3}); D_O is the oxygen diffusion coefficient (1.8×10^{-5} cm^2 s^{-1}); υ is the kinematic viscosity (0.01 cm^2 s^{-1}) [60].

The CV and LSV measurements were conducted in SP-50 potentiostat (Biologic S.A., Claix, France). All the potential readings were measured against Hg/HgO reference electrode. The reported current densities were based on the geometric area of the corresponding electrode configuration. Current interrupt method was used to measure the internal resistance. The LSV recorded were automatically compensated for iR drop by the workstation.

Results and discussion

Figure 1a shows the XRD patterns of the synthesized (LCMO) $La_{0.1}Ca_{0.9}MnO_3$ and Co_3O_4, respectively. The upper pattern belongs to the orthorhombic phase of $La_{0.1}Ca_{0.9}MnO_3$ (PDF number 01-086-1207). Each pattern apparently corresponds to the polycrystalline structure of the perovskite. No other impurity phases were observed such as Mn_2O_3/Mn_3O_4, La_2O_3, and CaO, demonstrating high purity of the synthesized sample. In the meantime (marked in ✦), peak splitting was observed due to the La substitution which induces the structural distortion to high degree of orthorhombicity, as similar splitting was reported in $La_{1-x}Ce_xMnO_3$ ($x = 0.2$) and oxygen-deficient $CaMnO_{3-\delta}$ ($\delta = 0.5$) [61, 62]. The major substitution of La^{3+} by Ca^{2+} cation in the A site and insertion of Mn^{3+} and Mn^{4+} with their respective oxygen vacancies may also affect the 2θ degrees with the lattice constants. The lower XRD pattern in Fig. 1a shows Co_3O_4 as the face-centered cubic structure of spinel (PDF number 01-074-1657). As no other peaks are observed in this pattern, the Co_3O_4 was found to be phase pure, as synthesized by the facile hydrolysis, precipitation, and oxidation reactions. The average crystallite sizes as determined by Scherrer equation was found to be 17 and 12 nm for $La_{0.1}Ca_{0.9}MnO_3$ and Co_3O_4, respectively, determined by the facets at (242) and (311) for LCMO and Co_3O_4, respectively.

The morphology of the synthesized powders (LCMO and Co_3O_4) is shown in Fig. 1b, c. The TEM image (Fig. 1b)

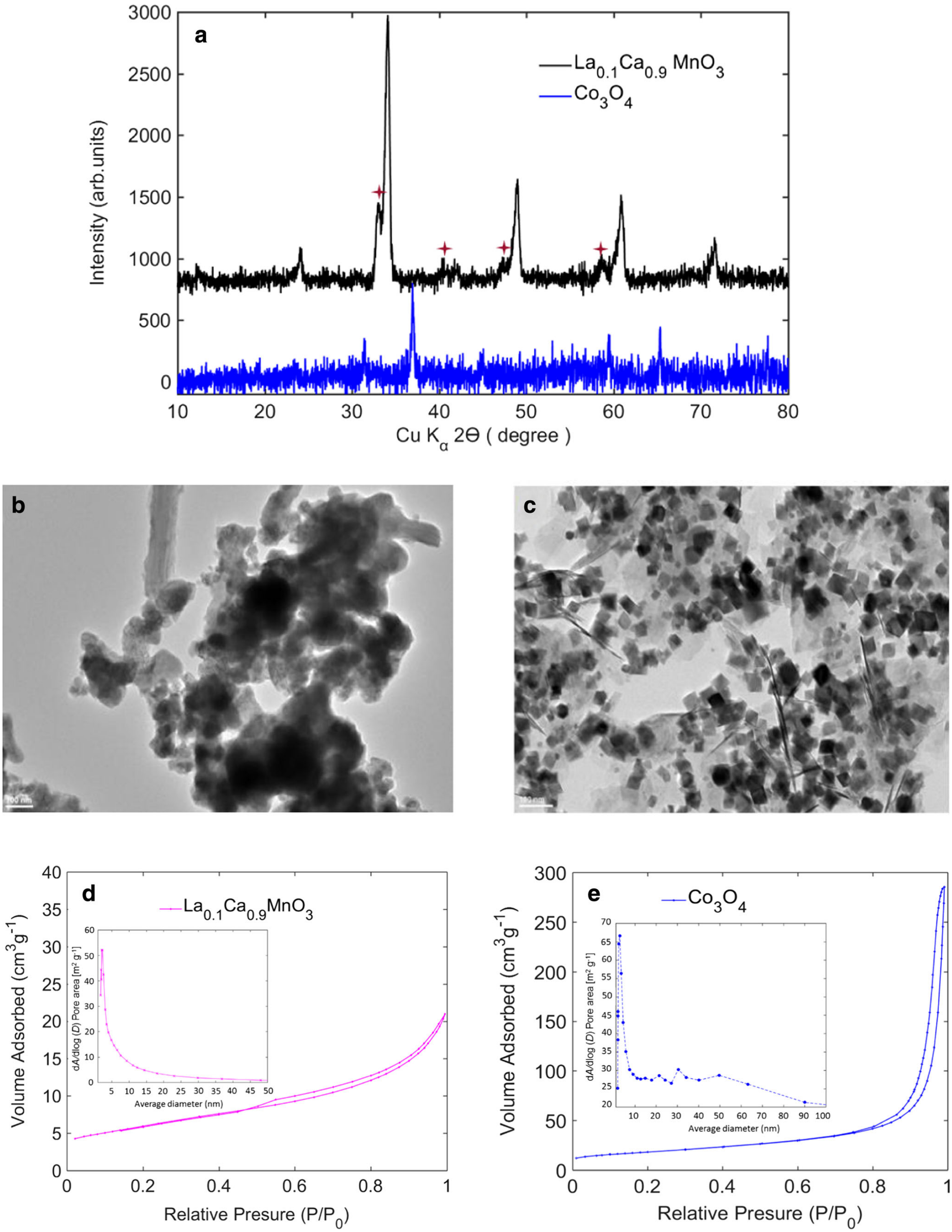

Fig. 1 **a** XRD pattern of $La_{0.1}Ca_{0.9}MnO_3$ and Co_3O_4. **b** TEM micrographs of $La_{0.1}Ca_{0.9}MnO_3$. **c** TEM micrographs of Co_3O_4. **d** Adsorption–desorption isotherm of $La_{0.1}Ca_{0.9}MnO_3$ and **e** Co_3O_4

depicts that the high-temperature synthesis with subsequent quenching results in crystalline, small, and interconnected particles. Although porous structure increases the mass transfer by enabling the reactants to reach the active sites easily, the particles are closely packed, dominated by less internal cavities. However, the crystalline and interconnected particles may reduce the charge transfer resistance in the electrochemical reactions.

Most of the particles of the spinel Co_3O_4 are in cubic form uniformly distributed nanocrystals having mostly less than 30 nm in size, whereas very few of them exist in platelet nanoneedle-like morphology with less than 5 nm in diameter (Fig. 1c). The topotactic synthesis process of Co_3O_4 follows the reactions in Eqs. 1 and 2, where the sol-precipitation of the nanocrystals of $Co(OH)_2$ is being transformed to nanowires according to Arhcer et al. [50] However, with vigorous stirring and longer reaction time by bubbling oxygen, oxidation of $Co(OH)_2$ takes place through crystallization/deposition/growth, enabling the conversion to nanocubes with much less distinct oblong nanowires. Thus, the nanocubes of Co_3O_4 with the phase purity can be prepared without templates, additives, and/or thermal treatment, rendering small particle sizes as demonstrated from the line broadening of the diffractograms.

Figure 1d and e shows the nitrogen adsorption–desorption isotherms and pore size distributions of $La_{0.1}Ca_{0.9}MnO_3$ and Co_3O_4, respectively. The $La_{0.1}Ca_{0.9}MnO_3$ isotherms are typically in the type IV isotherm with H3 hysteresis loops in accordance to IUPAC classification. This behavior is common for aggregates and agglomerates of particles with slit-shaped pores of microporous/mesoporous structure with very narrow size distribution dominating at 1.2 nm (inset Fig. 1d). This is in agreement with the observations in Fig. 1b and the average pore diameter of 6 nm, depicted in Table 1. Co_3O_4 is in the type III isotherm with H1 hysteresis loop, suggesting a dominantly microporous/mesoporous material, where most pores are aligned in the range of 1–10 nm with the peak appearing at 1.5 nm (inset Fig. 1e). Furthermore, mesopores emerge in the range of 10–100 nm, where increased N_2 uptake corresponding to capillary condensation was observed at the high relative pressure region (0.7 to 1) for Co_3O_4 having an average pore diameter of 27 nm (Table 1). Thus, the pore size distributions and pore volumes in both materials show characteristic features for gas–liquid phase reactions to be employed as cocatalysts. The results of the surface properties are summarized in Table 1. The BET specific surface areas were found to be 21 and 64 $m^2\ g^{-1}$ for $La_{0.1}Ca_{0.9}MnO_3$ and Co_3O_4, respectively. High surface area permits more interfacial contact between the electrolyte and catalyst. Moreover, it should be noted that more porous structures could facilitate the diffusion, adsorption, and transport of O_2 gas and hydrated ions in the solution [36].

Table 1 Surface properties of $La_{0.1}Ca_{0.9}MnO_3$ and Co_3O_4

Parameters	$La_{0.1}Ca_{0.9}MnO_3$	Co_3O_4
1. Surface area ($m^2\ g^{-1}$)	21	64
2. Pore volume ($cm^3\ g^{-1}$)	0.035	0.44
3. Average pore diameter (nm)	6	27

The electrocatalyst activity was first investigated by CV on LCMO and Co_3O_4 electrodes. Catalyst composition is shown in Table S2. CV was carried out on LCMO/graphite/Nafion on GC substrate in N_2-saturated 1 M KOH solution, and the redox activities are shown in Fig. 2. During the anodic scan, one big oxidation peak is observed at 0.04 V for $Mn^{+3} \rightarrow Mn^{+4}$ and another small peak with a shoulder at − 0.24 V vs. Hg/HgO in Fig. 2a most probably assigned to $Mn^{+2.67} \rightarrow Mn^{+3}$ reactions, respectively, which are much closer to the thermodynamic redox potential for these reactions at 0.089 and − 0.237 V vs. Hg/HgO [35, 61]. Further positive sweep resulted in the oxygen evolution beyond 0.45 V. In the case of reduction, single peak was observed at − 0.16 V vs. Hg/HgO, respectively, which is ascribed to Mn^{4+}/Mn^{3+} redox couple. $Mn^{3+} \rightarrow Mn^{2+}$ peak was not observed in the CV curve, which confirms that the material did not undergo further reduction. The voltammetric profiles are consistent to those found in the literature for manganese-based redox processes [63, 64]. Thus, the LCMO perovskite exhibits a dominantly Mn^{3+}/Mn^{4+} pair for the reduction and oxidation reactions with oxygen intercalated within its structure, and higher currents are believed to be obtained with the increase in the A site by Ca [58, 64].

Figure 2b shows the voltammogram of Co_3O_4/graphite/Nafion electrode in N_2-saturated 1 M KOH solution. In aqueous solutions following protonation and deprotonation, the cobalt oxides show two distinct redox pairs both at high and low potentials. During oxidation, peaks are observed at 0.26 and 0.56 V vs. Hg/HgO, respectively, with oxygen evolution to follow. The Co^{2+} starts oxidation prior to 0.26 V, and subsequently after 0.26 V, Co^{3+} is oxidized to Co^{4+}. On the reverse scan, reversible peaks were observed at 0.52 and 0.2 V vs. Hg/HgO which are related to Co^{4+}/Co^{3+} and Co^{3+}/Co^{2+}, respectively. The peaks attributed to the redox couple Co^{3+}/Co^{4+} show a formal redox potential of 0.54 V vs. Hg/HgO $[(E_{pa} + E_{pc}) / 2]$, having a peak potential difference of 40 mV in between, demonstrating a high amplitude and current density compared to the Co^{2+}/Co^{3+} pair. Similar redox couples in alkaline electrolytes were also reported by Singh et al. [65], although preparation of the spinel, morphology, loading, type of support, electrolyte concentration, etc. might affect the small differences of the anodic potentials. The spinel Co_3O_4 ($Co^{2+}[Co^{+3}{}_2]\ O_4$) has the mixed valence cobalt ion in its structure. These ions are progressively oxidized to produce both Co(III) and Co(IV) containing species as shown in Eqs. 5 and 6, which are catalytically supportive sites for the oxygen

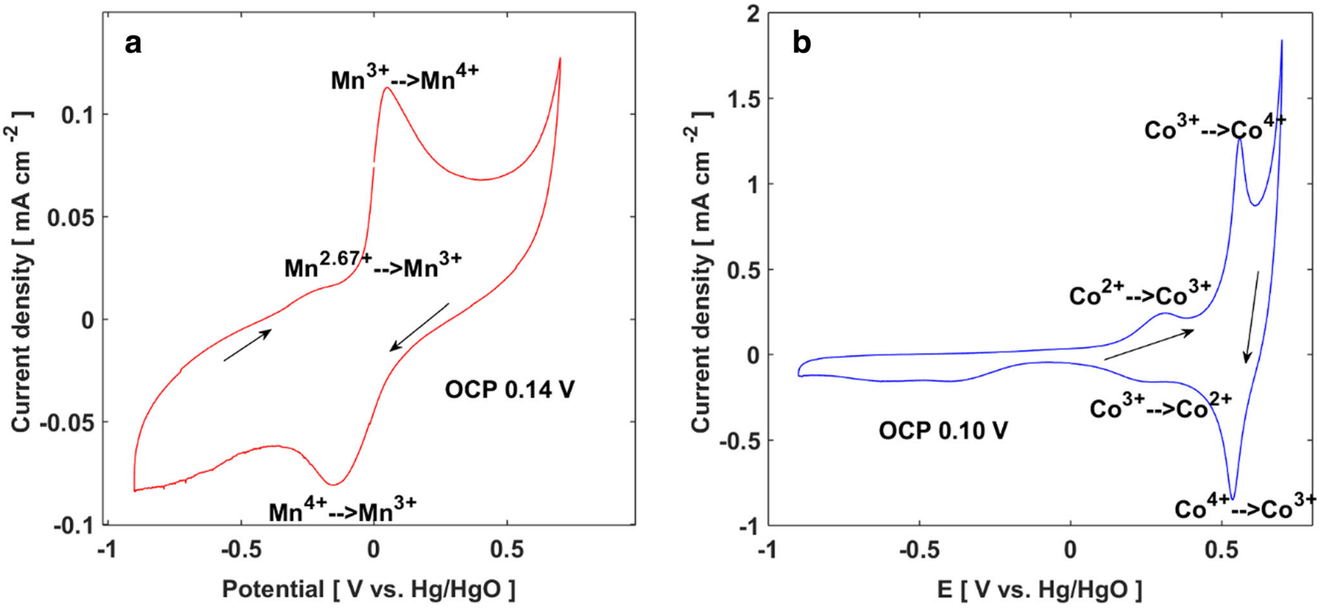

Fig. 2 **a** LCMO and **b** Co_3O_4 voltammogram on GC electrode with a sweep rate at 5 mV s^{-1}

evolution reaction [66, 67]. The redox processes at the spinel Co_3O_4 proceeds through the following mechanism [40]:

$Co_3O_4 + OH^- + H_2O \rightleftarrows 3CoOOH + e^-$ (5) $E_0 = 0.222$ V vs. Hg/HgO [65].

$CoOOH + OH^- \rightleftarrows CoO_2 + H_2O + e^-$ (6) $E_0 = 0.562$ V vs. Hg/HgO [65].

Figure 3 shows the LSV response of the sample whose mass loadings are tabulated in Table S2. For all the polarization curves, the iR and background capacitive current were corrected. The electrocatalytic activity for ORR shows the highest current density for the commercial Pt/C, and the least of all the catalysts was the spinel Co_3O_4. At the specific potential of − 0.3 V vs. Hg/HgO, the current densities for the catalysts investigated for ORR were − 2.2 for Pt, − 1.2 for LCMO + Co_3O_4, − 0.97 for LCMO, and − 0.3 mA cm^{-2} for Co_3O_4 displaying disparate activities. However, the Co_3O_4 upon addition of the LCMO, the Co_3O_4 increased its ORR activity by fourfold, implying a synergetic effect of the co-catalysts. The potential-dependent current densities at the rotation rate of 1600 rpm show a single sigmoid for the Pt and Co_3O_4-based gas diffusion electrodes (GDEs), while the LCMO and LCMO + Co_3O_4 show a dual sigmoidal character with a shift towards higher potentials for the later. These differences in the geometries of Fig. 3 might arise from the intrinsic oxygen reduction reaction mechanism depending on either direct pathway or indirect pathway or a combination of them. However, the OER for the catalysts were found to be in some cases on the contrary to the findings of the ORR, where the activities increased in the order of LCMO < Pt/C < LCMO + Co_3O_4 < Co_3O_4. Co_3O_4 has the highest oxygen evolution current of 1.3 mA cm^{-2} among the catalysts investigated. Due to the Co_3O_4 addition, the OER activity increased by threefold in the LCMO from 0.25 to 0.77 mA cm^{-2} at the given potential of 0.69 V vs. Hg/HgO. Thus, mixture of Co_3O_4 and LCMO resulted in improved performances for both the ORR and OER.

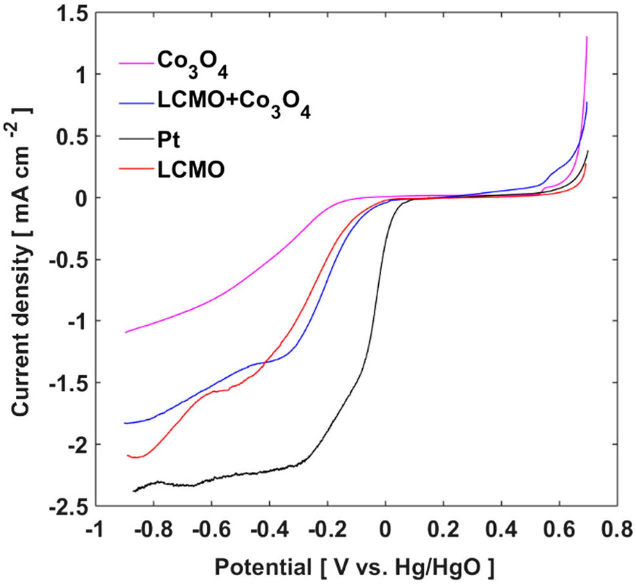

Fig. 3 LSV response of samples on GC electrode at 5 mV s^{-1}, rotation rate 1600 rpm in O_2-saturated 6 M KOH

The polarization curves by LSV on GC with scan rates at 5 mV s^{-1} with iR and background capacitive current correction both for ORR and OER for the different catalysts at low overpotentials are shown in Fig. 4a, b. Table 2 shows the Tafel slope values (mV decade^{-1}), calculated from the linear part of the OER polarization curve for all the samples. In the OER region, the Tafel slope in the overpotential region from 0.25 to

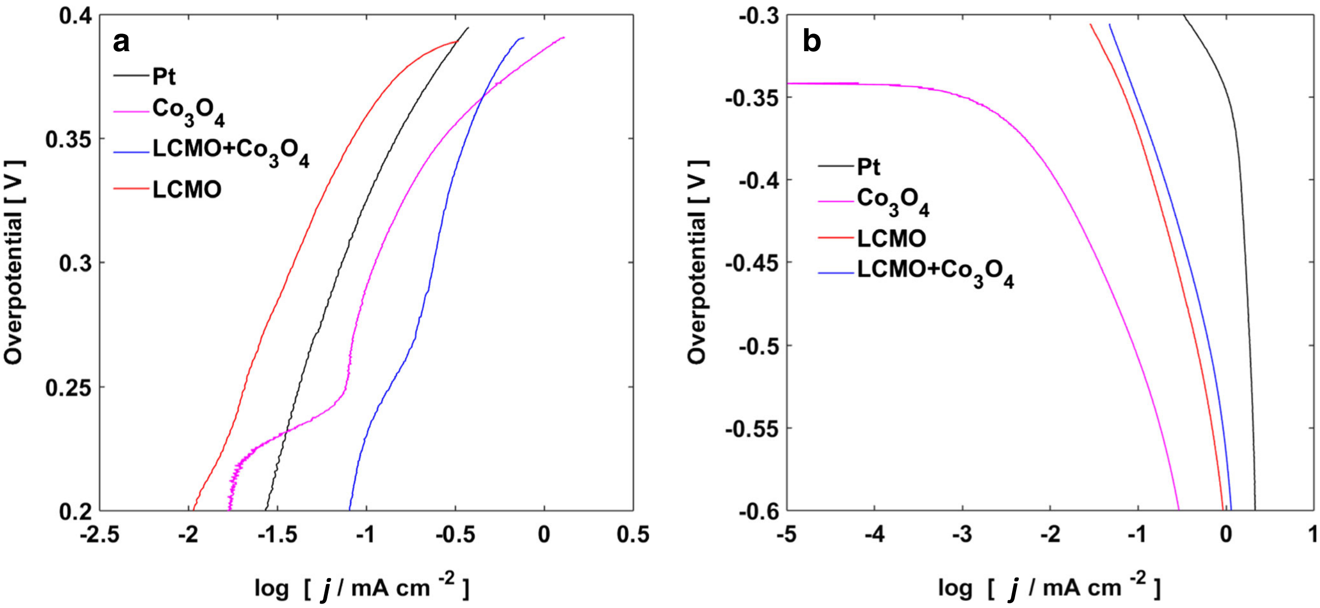

Fig. 4 Tafel plots. **a** OER and **b** ORR for the different catalysts

0.35 was used. Tafel slopes corresponding to 164, 56, 142, and 190 mV decade^{-1} were obtained for LCMO, Co_3O_4, LCMO + Co_3O_4, and Pt, respectively. Similar values were reported for Ca-based manganates and Co_3O_4 [33, 68]. Overall, the Pt/C showed the highest slope (190 mV decade^{-1}), while Co_3O_4 exhibited the lowest Tafel slope (56 mV decade^{-1}), implying increased kinetics for the OER. Addition of Co_3O_4 decreased substantially the Tafel slope value for LCMO from 164 to 142 mV decade^{-1}. The Tafel slope values for LCMO and LCMO mixed with Co_3O_4 are lower than for Pt/C, while for Co_3O_4, the value is close to 2.3 *RT/F*, suggesting that the variation of the Tafel slopes for these catalysts may be attributed or related to the main causes for the variations in OH^- films, surface coverage by adsorbed oxygen species, surface structure and electronic properties, gas bubble formation, and entrapment [69, 70]. Besides, the lower Tafel slope of the Co_3O_4-based electrodes is probably associated with the electrophilic and deprotonating properties of the mixed valence cobalt ions causing efficient oxygen evolution as shown in Fig. 2b and Eqs. 5 and 6. On the ORR side, all the samples showed two distinct linear regions, which are related to the potential-dependent surface coverage of the adsorbed species and interactions of molecular oxygen with the metal cations. Tafel slope values are closer to 30 and 120 mV decade^{-1} for low and high overpotential regions, respectively. LCMO with Co_3O_4 shows slightly reduced current at high overpotentials with higher Tafel feature than the LCMO, suggesting that the effect of Co_3O_4 addition did alter the kinetics somehow as its OR is less distinct as also shown in Fig. 3.

Table 2 Tafel slopes of OER and ORR

Electrode	Slope (mV decade^{-1})		
	OER	ORR low η	ORR high η
LCMO	164	37	122
Co_3O_4	56	38	119
LCMO + Co_3O_4	142	28	144
Pt	190	30	128

In order to elucidate and determine the number of electrons exchanged and compare among the different catalysts prepared, Fig. S1a–d shows the RDE voltammograms for the compositions shown in Table S2. The RDE measurements were performed by linear sweep voltammetry mode at 2 mV s^{-1} with various rotation rates in O_2-saturated 1 M KOH. This setup eliminates the mass transfer limitations and hence permitting us to investigate the kinetically controlled ORR. In all the catalysts, the limiting current densities (j_L) increased with the rotation rates, which is ascribed to the thinner diffusion layer that allows faster transport of oxygen to the electrode surface as function of the rotation rate. The polarization curves of the LCMO-based electrodes do possess bisigmoidal shapes.

Figure S1a shows the electrode containing LCMO catalyst polarization curve at different rotation rates, and the inset figure shows the Koutecky–Levich (K–L) plot. For the LCMO catalyst, the limiting current density (j_L) increased by twofold from 1.1 mA cm^{-2} when the rotation rate increased from 500 to 2500 rpm. Co_3O_4 (Fig. S1b) and LCMO + Co_3O_4 (Fig. S1c) electrodes exhibited lower current densities at the same rotation rate and potential. It is well known that without carbon support (high surface area carbon, reduced graphene oxide) and metal additives, pure Co_3O_4 having low conductivity shows low ORR activity [5, 44] as the graphite content is low in this study. The K–L plots (j^{-1} vs. ω^{-1}) (inset in Fig. S1a–c) for all the three catalysts were parallel and linear at different potentials, which means that the ORR reaction follows the first-order kinetics. Figure S1d shows Pt polarization curves, which is a well-known catalyst for ORR. Its limiting current densities were much higher than the LCMO, Co_3O_4, and LCMO + Co_3O_4-based electrodes, and its K–L slopes at different potentials were near identical to each other compared to the well-separated curves of Fig. S1a–c.

Figure 5 shows the number of electrons transferred during the ORR, which is an important parameter to determine the intrinsic catalyst activity and mechanism. The number of electrons transferred as function of the potentials was 1.75 to 2 for Co_3O_4 and 2.75 to 3.2 for LCMO and Co_3O_4 + LCMO, respectively. The number of electrons transferred for the Pt-based electrode was between 3.6 and 4; similar values were reported [71]. While the Co_3O_4-based electrode showed the number of transferred electrons at 1.75 to 2 [72]. Therefore, the oxygen reduction is to proceed through the $2e^-$ peroxide pathway. Upon Co_3O_4 addition to the LCMO, however, the number of electrons involved for the ORR did not alter too much, implying that the ORR occurs simultaneously through both the $4e^-$ and $2e^-$ pathways as depicted in the bisigmoidal behavior of the shape of the polarization curves [73] in Fig. 3. Our LCMO and Co_3O_4 + LCMO containing samples delivered 3 to $3.2e^-$, which were closer to reported $CaMnO_3$ material with $3.5e^-$ [35]. However, through the addition of the conductive carbon and/or Co_3O_4, the mechanism for oxygen reduction is expected to be reduced to ca. 2. Moreover, in the mixture of Co_3O_4 + LCMO electrode, the ORR is able to proceed on par with LCMO electrode. Oxygen reduction in alkaline solution on carbon/graphite and Co_3O_4 appears to pass through the intermediate peroxide scheme, where in the former case, peroxyl ion concentration increases significantly resulting in far beyond the reversible oxygen potential. Thus, the advantage of the co-catalyst/mixed catalyst of LCMO may infuse the scheme towards the direct reduction through the 4e as a strategy for the synergetic effect of increasing the catalytic activity [74, 75].

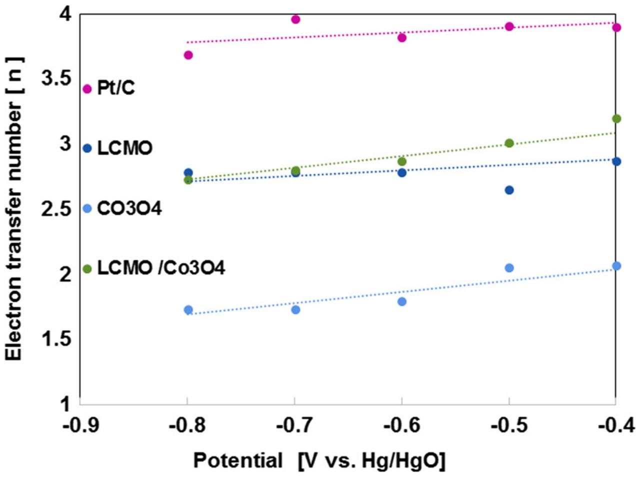

Fig. 5 Number of electrons transferred at different potentials

Electrode bifunctional stability is an important parameter, which defines the lifetime of the catalyst/electrode for application for example in metal–air batteries with several charge and discharge cycles. This characteristic was investigated for different single or mixed catalysts by subjecting them to 50 continuous cycles by potential sweeps between − 0.35 and 0.70 V vs. Hg/HgO for both ORR and OER. Table S1 shows the electrode compositions with respective loadings of the catalysts used in the stability test as compared to the relatively low catalyst loadings used in the RDE study used in Table S2. Figure 6a–d shows ORER profiles of the GDEs for the respective catalysts.

The LCMO containing electrodes depicts pseudocapacitive rectangular current–voltage response, which are typical to multivalent Mn compounds. This capacitance arises due to the K^+ and OH^- ion electrosorption on the Mn ion oxygen vacancy sites [76]. Figure 6a shows the voltammogram of the LCMO/graphite GDE. In the first cycle, LCMO exhibited high current densities corresponding to 29 and 59 mA cm^{-2} for the OER and ORR, respectively. After 50 cycles, the current densities for the OER and ORR of the same electrode dropped to 17 and 47 mA cm^{-2}. On further charge and discharge cycles, the OER potential shifted to positive potential values, increasing by 80 mV from the initial 0.67 V vs. Hg/HgO. Thus, the current density for the OER was considerably decreased, while maintaining minor decline for the ORR, implying that the LCMO shows a higher activity for this later reaction. Figure 6b shows the voltammogram of the Co_3O_4/graphite/GDE. The first cycle delivered 61 and 8 mA cm^{-2} for OER and ORR, respectively. Upon successive cycles (10–50 cycles), the currents increased substantially for the OER and slightly for the ORR and were stabilized at 75 and 10 mA cm^{-2}. This is a significant outcome, where both the oxygen evolution and reduction were shown to be enhanced by more than 20%, albeit the current density for the ORR was lower by more than a factor of 7 than for the OER.

The perovskite LCMO shown in Fig. 6a compared to spinel Co_3O_4 in Fig. 6b delivered high ORR current density, while on the other hand, Co_3O_4 has stable oxygen evolution performance. Therefore, combining the two catalysts has interesting features for the bifunctional OER/ORR, pertaining to their potential–current characteristics during the repeated cycles.

Figure 6c shows the voltammogram of the LCMO and Co_3O_4 mixed electrode performance. In the first cycle, the OE and OR current for the respective reactions was 58 and 45 mA cm^{-2}, which were stabilized after 30 cycles and finally displayed at the 50th cycle at 48 and 37 mA cm^{-2}. Remarkably, the ORER current densities were found to be still high and constant after the extended 50 cycles. The addition of Co_3O_4 resulted in the initial increase of the current density for OER by a factor of 2 compared to the LCMO-based GDE in Fig. 6a. However, the current density for the ORR was abated by about 0.8 times. The LCMO-based electrode showed a 41% current density decay from the 1st cycle to the 50th cycle

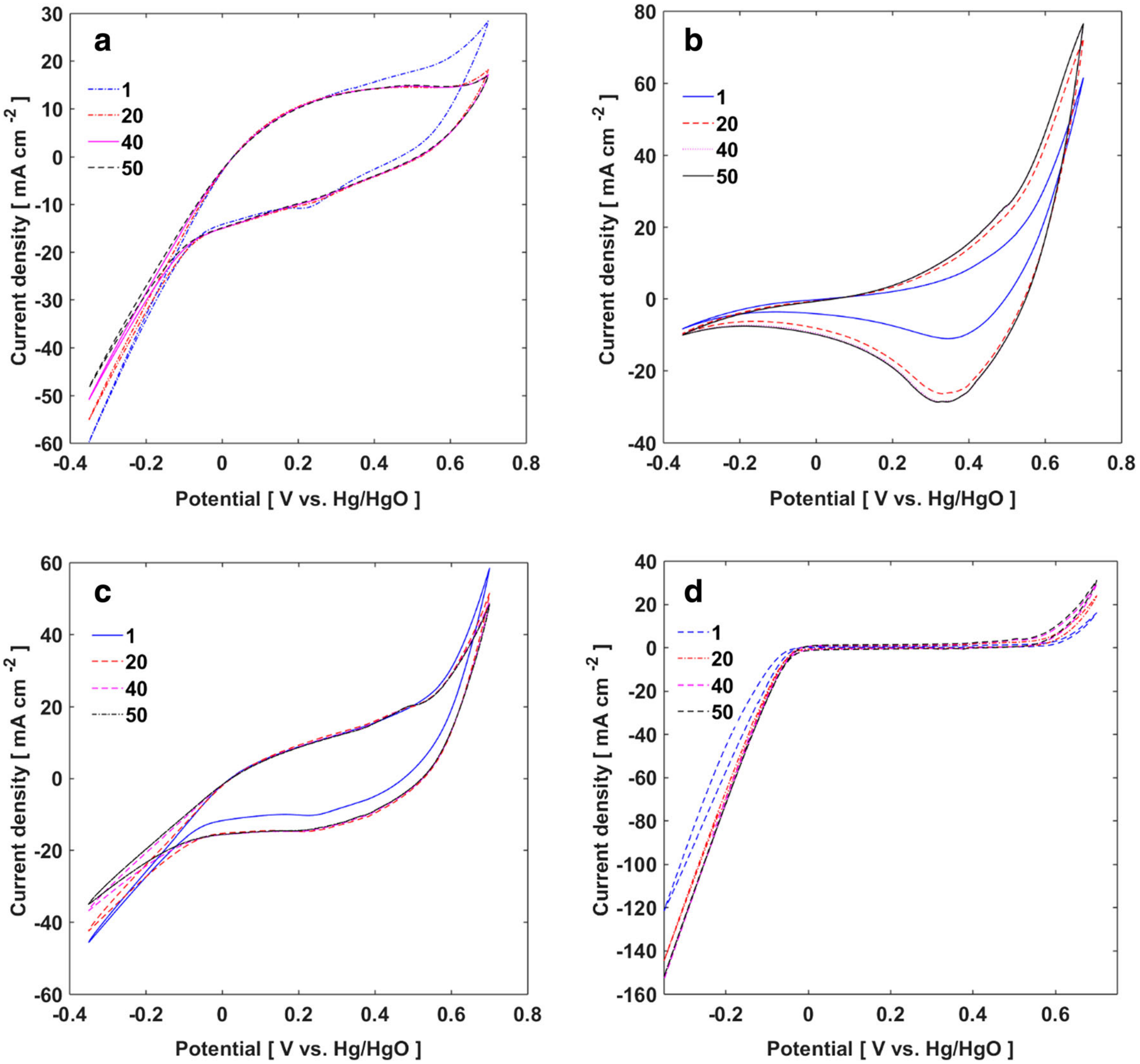

Fig. 6 Voltammograms for stability tests of the GDEs **a** LCMO, **b** Co_3O_4, **c** LCMO + Co_3O_4, and **d** Pt/Vulcan XC-72 in O_2-saturated 6 M KOH at 5 mV s^{-1}

in the OER direction, whereas addition of Co_3O_4 in these mixed oxide catalysts resulted in a 17% decrease. In the mixed LCMO and Co_3O_4, the electrode had 23 and 10 mg cm^{-2} for respective oxide catalyst, taken in separate mode but overall having 33 mg cm^{-2}, whereas the loadings in the separately prepared LCMO and Co_3O_4-based electrodes were 34 and 32 mg cm^{-2}, respectively. Though the amount of Co_3O_4 in the mixed type of electrode was lower than its corresponding single oxide electrode, the bifunctional performance hitherto shown supports the synergistic effects of LCMO and Co_3O_4 combined together. Although the ORR performance for many perovskites is considered to be low, $La_{0.1}Ca_{0.9}MnO_3$ has shown to have a high catalytic activity for this reaction among the candidate perovskites studied and stable OER was noted for above 170 cycles for GDEs [36]. The effects may be ascribed to the physicochemical nature of the perovskite and the synthesis method used. Furthermore, the enhancement of the OER may also be attributed to the nanoparticle sizes of the Co_3O_4, having high surface area and porous structure, prepared by the stepwise precipitation and oxidation.

Figure 6d presents the bifunctional activity of the commercial ETEK 20% Pt on Vulcan XC-72 electrode used as a benchmark to compare the electrode performance. Pt showed the highest oxygen reduction current (120 mA cm^{-2}) among the catalysts studied during the first cycle, which then gradually increased to 152 mA cm^{-2}. In addition, its OE performance was 16 mA cm^{-2} at the initial cycle, which then increased to 31 mA cm^{-2} at the 50th cycle. However, upon repeated cycles, the carbon support in the Pt-based electrode culminated in dissolution or corrosion turning the electrolyte into brownish color due to the high potentials (> 0.6 V vs. Hg/HgO) during the oxygen evolution. This phenomenon was not observed in the other catalytic materials as the support/conductive material was a high surface area graphite and its composition was four times lower than in the Pt-based electrode.

Figure 7 shows the OER/ORR mass activities of the GC and GDE electrodes. Major differences between the GC and GDE electrodes were the mass loadings, the hydrodynamics, electrolyte concentration, and conductivity. On the GC electrodes, the mass loading varied between 0.47 and 0.59 mg cm^{-2} and the rotation was 1600 rpm. On the other hand, the mass loading of the GDEs was in the range of 32–35 mg cm^{-2}, and the electrode was stationary. Overall, the GC electrodes showed a small mass activity increase compared to the GDE electrode especially on the ORR side. The reason for this might be the accelerated mass transfer in the RDE experiment. The OER mass activities increased in the order of LCMO < LCMO + Co_3O_4 < Co_3O_4. The ORR followed the reverse trend as LCMO > LCMO + Co_3O_4 > Co_3O_4, which confirms that Co_3O_4 addition increases the OER activity on LCMO, while in the meantime, the ORR activity was not altered significantly. Co_3O_4 addition to the LCMO resulted in 1.3 and − 1.98 A g^{-1} on the OER and ORR side, respectively. These values are comparable to the reported similar perovskite materials [33, 77]. Interestingly, based on the mass activities, the OER does not show big variations between both the GC, while the rotation rate for the ORR influences to great extent of comparing a miniature geometric area to a bigger gas diffusion electrode.

Figure 8 presents XRD spectra of the freshly prepared and the corresponding electrodes after 50 cycles. The Co_3O_4 containing electrode show a mixture of the phases having CoO and Co_3O_4 structure, where the former is produced during the sintering procedure and thus reduction of Co_3O_4 at 320 °C in N_2 flow. After repeated 50 cycles, however, the Co^{2+} tended to oxidize and could no longer be identified in the diffractograms. In the LCMO containing material, no extra phase corresponding to manganese or lanthanum hydroxides was observed and the crystallite sizes were not observed to change according to the diffractograms. This confirms that the electrodes are structurally stable during the continuous bifunctional OER/ORR operation. Overall, Co_3O_4 addition imparts the high and stable OER/ORR current densities.

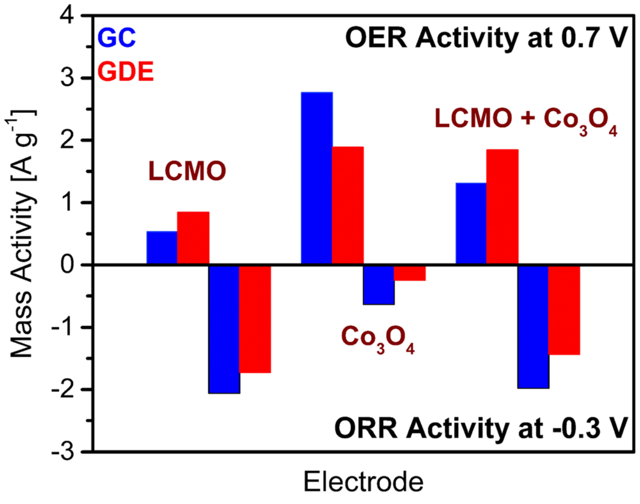

Fig. 7 Mass activities on the GC and GDE (data extracted from Figs. 3 and 6)

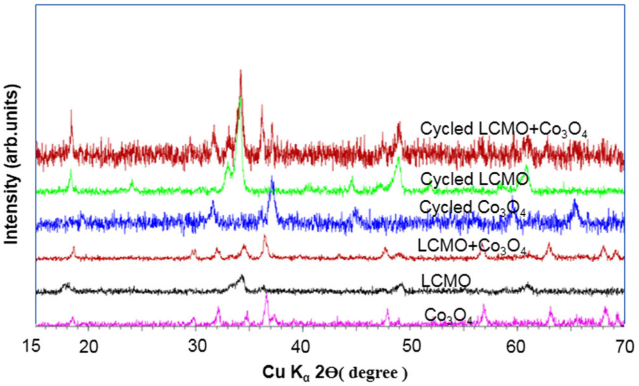

Fig. 8 XRD patterns of fresh electrodes and after 50 cycles

To further understand the electrodes' morphological changes, scanning electron microscopy was performed at different magnifications on the fresh and on electrodes containing the catalysts LCMO + Co_3O_4, as well as Co_3O_4, and these are shown in Figs. S3 and S4. For comparison, SEM images of the constituent powder samples are also shown in Fig. S2. Figure S3 shows that the LCMO + Co_3O_4 electrode surface morphology at the initial stage (a, b) and after 50 cycles (c, d). After 50 cycles, Fig. S3c, d shows resemblance to the initial images in Fig. S3a, b without no significant change in both particle size and morphology. However, slight particle roughening was observed at higher magnification (Fig. S3d), which might be due to the presence of the KOH leading to crystals on the particles. Similar changes were also found on the only Co_3O_4 containing electrodes as shown in Fig. S4d. Overall, no major morphological changes were observed on these two samples, which might confirm that the catalysts were stable during the electrochemical cycling. Thus, the SEM together with the XRD results shows that the catalysts are structurally and crystallographically fit for the bifunctional activity of the OER/ORR during the length of the electrochemical operation.

The high activity of OER/ORR and durability of perovskite and Co_3O_4 mixed catalyst indicate that as a non-noble metal, earth-abundant and low-cost bifunctional catalyst can be used for application in metal–air batteries. The performance could be related to primarily e_g (< 1) electron occupancy of the Mn ion (+ 3.7 and oxygen non-stoichiometry) and Co e_g (> 1) mixed valence for the high OER and secondly the ionic conductivity of LCMO. These features make LCMO and Co_3O_4 mixed catalyst as an excellent catalyst for bifunctional catalyst for OER/ORR.

Conclusion

Co_3O_4-nanosized particles were synthesized successfully using a facile method. The resultant nanomaterials of both the spinel and the perovskite LCMO showed interconnected networks, having uniform particle size and high surface area with varied pore volumes and pore size distributions. The electrode kinetic studies of $La_{0.1}Ca_{0.9}MnO_3$ mixed with Co_3O_4 showed improved bifunctional activity for both the ORR and OER. The spinel Co_3O_4 proceeds through the $2e^-$ pathway, while $La_{0.1}Ca_{0.9}MnO_3$ mixed with Co_3O_4 promotes a mixed pathway of both the 2e and 4e. Their bifunctional activity and stability in 6 M KOH on GDE showed that $La_{0.1}Ca_{0.9}MnO_3$ mixed with Co_3O_4 showed durable and high performances compared to the single-phase electrodes of the respective catalysts. The OER mass activities were found to be similar on both the GC and GDE, although there are minor differences in the ORR due to operations and other physical parameters. The OER and ORR mass activities for the mixed catalyst were found to be 1.3 and 1.98 A g^{-1}, respectively, exhibiting a quasi-reversible and effective catalytic response compared to similar single or mixed phase catalysts. The high activity of the mixed electrodes may be attributed to the structural robustness and synergistic effect. Ex situ XRD measurements of the cycled gas diffusion electrodes were shown to be structurally stable with no major phase transformation. The nanoblending and casting of two different catalysts such as in this study of the LCMO/Co_3O_4 may be considered as a strategy and a way forward for solving the high overpotentials encountered in both the OER/ORR and find applications in many electrochemical energy conversions and storage.

Acknowledgements This work is supported by Swedish energy agency.

References

1. International Energy Agency, WEO (2015)
2. EMC (2015) The outlook for energy: a view to 2040
3. Rogelj J, Luderer G, Pietzcker RC, Kriegler E, Schaeffer M, Krey V, Riahi K (2015) Energy system transformations for limiting end-of-century warming to below 1.5 [deg]C. Nat Clim Chang 5(6): 519–527. https://doi.org/10.1038/nclimate2572
4. U. N secretariat. Paris Agreement, Decision 1/CP.21, Article 17
5. Zhao S, Rasimick B, Mustain W, Xu H (2017) Highly durable and active Co_3O_4 nanocrystals supported on carbon nanotubes as bifunctional electrocatalysts in alkaline media. Appl Catal B Environ 203:138–145. https://doi.org/10.1016/j.apcatb.2016.09.048
6. Technology Roadmap: Solar Photovoltaic Energy. (7 October 2014.). International Energy Agency (2014) "Technology Roadmap: Solar Photovoltaic Energy" (PDF) IEA Archived (PDF) from the original on 7 October 2014 Retrieved 7 October 2014
7. Salvador-Pascual JJ, Citalán-Cigarroa S, Solorza-Feria O (2007) Kinetics of oxygen reduction reaction on nanosized Pd electrocatalyst in acid media. J Power Sources 172(1):229–234. https://doi.org/10.1016/j.jpowsour.2007.05.093
8. Larcher D, Tarascon JM (2015) Towards greener and more sustainable batteries for electrical energy storage. Nat Chem 7(1):19–29. https://doi.org/10.1038/nchem.2085
9. Akinyele DO, Rayudu RK (2014) Review of energy storage technologies for sustainable power networks. Sustain Energy Technol Assess 8:74–91. https://doi.org/10.1016/j.seta.2014.07.004
10. Öjefors L, Carlsson L (1978) An iron—air vehicle battery. J Power Sources 2(3):287–296. https://doi.org/10.1016/0378-7753(78)85019-8
11. Neburchilov V, Wang H, Martin JJ, Qu W (2010) A review on air cathodes for zinc–air fuel cells. J Power Sources 195(5):1271–1291. https://doi.org/10.1016/j.jpowsour.2009.08.100
12. Narayanan SR, Prakash GKS, Manohar A, Yang B, Malkhandi S, Kindler A (2012) Materials challenges and technical approaches for realizing inexpensive and robust iron–air batteries for large-scale energy storage. Solid State Ionics 216:105–109. https://doi.org/10.1016/j.ssi.2011.12.002
13. Gorlin Y, Jaramillo TF (2010) A bifunctional nonprecious metal catalyst for oxygen reduction and water oxidation. J Am Chem Soc 132(39):13612–13614. https://doi.org/10.1021/ja104587v
14. Song W, Ren Z, Chen S-Y, Meng Y, Biswas S, Nandi P, Elsen HA, Gao P-X, Suib SL (2016) Ni- and Mn-promoted mesoporous Co_3O_4: a stable bifunctional catalyst with surface-structure-dependent activity for oxygen reduction reaction and oxygen evolution reaction. ACS Appl Mater Interfaces 8(32):20802–20813. https://doi.org/10.1021/acsami.6b06103
15. Chen D, Chen C, Baiyee ZM, Shao Z, Ciucci F (2015) Nonstoichiometric oxides as low-cost and highly-efficient oxygen reduction/evolution catalysts for low-temperature electrochemical devices. Chem Rev 115(18):9869–9921. https://doi.org/10.1021/acs.chemrev.5b00073
16. Karlsson G (1985) Perovskite catalysts for air electrodes. Electrochim Acta 30(11):1555–1561. https://doi.org/10.1016/0013-4686(85)80019-0
17. Osgood H, Devaguptapu SV, Xu H, Cho J, Wu G (2016) Transition metal (Fe, Co, Ni, and Mn) oxides for oxygen reduction and evolution bifunctional catalysts in alkaline media. Nano Today 11(5):601–625. https://doi.org/10.1016/j.nantod.2016.09.001
18. Jörissen L (2006) Bifunctional oxygen/air electrodes. J Power Sources 155(1):23–32. https://doi.org/10.1016/j.jpowsour.2005.07.038
19. Zhu H, Zhang P, Dai S (2015) Recent advances of lanthanum-based perovskite oxides for catalysis. ACS Catal 5(11):6370–6385. https://doi.org/10.1021/acscatal.5b01667
20. Li Y, Dai H (2014) Recent advances in zinc-air batteries. Chem Soc Rev 43(15):5257–5275. https://doi.org/10.1039/C4CS00015C
21. Lee Y, Suntivich J, May KJ, Perry EE, Shao-Horn Y (2012) Synthesis and activities of rutile IrO_2 and RuO_2 nanoparticles for oxygen evolution in acid and alkaline solutions. J Phys Chem Lett 3(3):399–404. https://doi.org/10.1021/jz2016507
22. Chen J, Lim B, Lee EP, Xia Y (2009) Shape-controlled synthesis of platinum nanocrystals for catalytic and electrocatalytic applications. Nano Today 4(1):81–95. https://doi.org/10.1016/j.nantod.2008.09.002
23. Morozan A, Jousselme B, Palacin S (2011) Low-platinum and platinum-free catalysts for the oxygen reduction reaction at fuel cell cathodes. Energy Environ Sci 4(4):1238–1254. https://doi.org/10.1039/c0ee00601g
24. McKerracher RD, Alegre C, Baglio V, Aricò AS, Ponce de León C, Mornaghini F, Rodlert M, Walsh FC (2015) A nanostructured

bifunctional Pd/C gas-diffusion electrode for metal-air batteries. Electrochim Acta 174:508–515. https://doi.org/10.1016/j.electacta.2015.06.001

25. Hyodo T, Hayashi M, Miura N, Yamazoe N (1996) Catalytic activities of rare-earth manganites for cathodic reduction of oxygen in alkaline solution. J Electrochem Soc 143(11):L266–L267. https://doi.org/10.1149/1.1837229
26. Sunarso J, Torriero AAJ, Zhou W, Howlett PC, Forsyth M (2012) Oxygen reduction reaction activity of la-based perovskite oxides in alkaline medium: a thin-film rotating ring-disk electrode study. J Phys Chem C 116(9):5827–5834. https://doi.org/10.1021/jp211946n
27. Suntivich J, May KJ, Gasteiger HA, Goodenough JB, Shao-Horn Y (2011) A perovskite oxide optimized for oxygen evolution catalysis from molecular orbital principles. Science 334(6061):1383–1385. https://doi.org/10.1126/science.1212858
28. Suntivich J, Gasteiger HA, Yabuuchi N, Nakanishi H, Goodenough JB, Shao-Horn Y (2011) Design principles for oxygen-reduction activity on perovskite oxide catalysts for fuel cells and metal-air batteries. Nat Chem 3(8):647–647. https://doi.org/10.1038/nchem.1093
29. Hong WT, Risch M, Stoerzinger KA, Grimaud A, Suntivich J, Shao-Horn Y (2015) Toward the rational design of non-precious transition metal oxides for oxygen electrocatalysis. Energy Environ Sci 8(5):1404–1427. https://doi.org/10.1039/C4EE03869J
30. Read MSD, Saiful Islam M, Watson GW, King F, Hancock FE (2000) Defect chemistry and surface properties of LaCoO. J Mater Chem 10(10):2298–2305. https://doi.org/10.1039/b002168g
31. Liu Y, Dong J, Xing DY (1998) Magnetic phase diagram of perovskite Mn oxides at T=0. Eur Phys J B 3(2):185–188. https://doi.org/10.1007/s100510050301
32. Han X, Zhang T, Du J, Cheng F, Chen J (2013) Porous calcium-manganese oxide microspheres for electrocatalytic oxygen reduction with high activity. Chem Sci 4(1):368–376. https://doi.org/10.1039/C2SC21475J
33. Kim J, Yin X, Tsao K-C, Fang S, Yang H (2014) $Ca_2Mn_2O_5$ as oxygen-deficient perovskite electrocatalyst for oxygen evolution reaction. J Am Chem Soc 136(42):14646–14649. https://doi.org/10.1021/ja506254g
34. Calegaro ML, Lima FHB, Ticianelli EA (2006) Oxygen reduction reaction on nanosized manganese oxide particles dispersed on carbon in alkaline solutions. J Power Sources 158(1):735–739. https://doi.org/10.1016/j.jpowsour.2005.08.048
35. Celorrio V, Calvillo L, Dann E, Granozzi G, Aguadero A, Kramer D, Russell AE, Fermin DJ (2016) Oxygen reduction reaction at $La_xCa_{1-x}MnO_3$ nanostructures: interplay between A-site segregation and B-site valency. Catal Sci Technol 6(19):7231–7238. https://doi.org/10.1039/C6CY01105E
36. Bursell M, Pirjamali M, Kiros Y (2002) $La_{0.6}Ca_{0.4}CoO_3$, $La_{0.1}Ca_{0.9}MnO_3$ and $LaNiO_3$ as bifunctional oxygen electrodes. Electrochim Acta 47(10):1651–1660. https://doi.org/10.1016/S0013-4686(02)00002-6
37. Morimoto H, Kamata M, Esaka T (1996) Nonstoichiometry of sintered oxide $Ca_{0.9}La_{0.1}MnO_{3-\delta}$ and its cathodic properties in alkaline solutions. J Electrochem Soc 143(2):567–570. https://doi.org/10.1149/1.1836481
38. Morimoto H, Esaka T, Takai S (1997) Properties of the perovskite-type oxide ceramic $Ca_{1-x}La_{2x}3MnO_{3-\delta}$ as the cathode active materials in alkaline batteries. Mater Res Bull 32(10):1359–1366. https://doi.org/10.1016/S0025-5408(97)00113-X
39. Binitha NN, Suraja PV, Yaakob Z, Resmi MR, Silija PP (2010) Simple synthesis of Co3O4 nanoflakes using a low temperature sol–gel method suitable for photodegradation of dyes. J Sol-Gel Sci Techn 53(2):466–469. https://doi.org/10.1007/s10971-009-2098-8
40. Meng T, Xu Q-Q, Wang Z-H, Li Y-T, Gao Z-M, Xing X-Y, Ren T-Z (2015) Co_3O_4 nanorods with self-assembled nanoparticles in queue for supercapacitor. Electrochim Acta 180:104–111. https://doi.org/10.1016/j.electacta.2015.08.085
41. Huang Y, Zhang M, Liu P, Wang L, Cheng F (2016) Improved performance of cobalt-based spinel by the simple solvothermal method as electrocatalyst for oxygen reduction reaction in alkaline solution. Ionics:1–8
42. Singh SK, Dhavale VM, Kurungot S (2015) Surface-tuned Co_3O_4 nanoparticles dispersed on nitrogen-doped graphene as an efficient cathode electrocatalyst for mechanical rechargeable zinc–air battery application. ACS Appl Mater Interfaces 7(38):21138–21149. https://doi.org/10.1021/acsami.5b04865
43. Ramsundar R, Debgupta J, Pillai V, Joy P (2015) Co_3O_4 nanorods—efficient non-noble metal electrocatalyst for oxygen evolution at neutral pH. Electrocatalysis 6(4):331–340. https://doi.org/10.1007/s12678-015-0263-0
44. Amin HMA, Baltruschat H, Wittmaier D, Friedrich KA (2015) A highly efficient bifunctional catalyst for alkaline air-electrodes based on a Ag and Co_3O_4 hybrid: RRDE and online DEMS insights. Electrochim Acta 151:332–339. https://doi.org/10.1016/j.electacta.2014.11.017
45. Aghazadeh M (2012) Electrochemical preparation and properties of nanostructured Co_3O_4 as supercapacitor material. J Appl Electrochem 42(2):89–94. https://doi.org/10.1007/s10800-011-0375-z
46. Liu W, Yang H, Zhao L, Liu S, Wang H, Chen S (2016) Mesoporous flower-like Co_3O_4/C nanosheet composites and their performance evaluation as anodes for lithium ion batteries. Electrochim Acta 207:293–300. https://doi.org/10.1016/j.electacta.2016.05.006
47. Esswein AJ, McMurdo MJ, Ross PN, Bell AT, Tilley TD (2009) Size-dependent activity of Co_3O_4 nanoparticle anodes for alkaline water electrolysis. J Phys Chem C 113(33):15068–15072. https://doi.org/10.1021/jp904022e
48. Liang Y, Li Y, Wang H, Zhou J, Wang J, Regier T, Dai H (2011) Co_3O_4 nanocrystals on graphene as a synergistic catalyst for oxygen reduction reaction. Nat Mater 10(10):780–786. https://doi.org/10.1038/nmat3087
49. Jiang J, Shi W, Song S, Hao Q, Fan W, Xia X, Zhang X, Wang Q, Liu C, Yan D (2014) Solvothermal synthesis and electrochemical performance in super-capacitors of Co_3O_4/C flower-like nanostructures. J Power Sources 248:1281–1289. https://doi.org/10.1016/j.jpowsour.2013.10.046
50. Lou XW, Deng D, Lee JY, Feng J, Archer LA (2008) Self-supported formation of needlelike Co_3O_4 nanotubes and their application as lithium-ion battery electrodes. Adv Mater 20(2):258–262. https://doi.org/10.1002/adma.200702412
51. Wittmaier D, Aisenbrey S, Wagner N, Friedrich KA (2014) Bifunctional, carbon-free nickel/cobalt-oxide cathodes for lithium-air batteries with an aqueous alkaline electrolyte. Electrochim Acta 149:355–363. https://doi.org/10.1016/j.electacta.2014.10.088
52. Song Z, Zhang Y, Liu W, Zhang S, Liu G, Chen H, Qiu J (2013) Hydrothermal synthesis and electrochemical performance of Co3O4/reduced graphene oxide nanosheet composites for supercapacitors. Electrochim Acta 112:120–126. https://doi.org/10.1016/j.electacta.2013.08.155
53. Xu J, Gao P, Zhao TS (2012) Non-precious Co3O4 nano-rod electrocatalyst for oxygen reduction reaction in anion-exchange membrane fuel cells. Energy Environ Sci 5(1):5333–5339. https://doi.org/10.1039/C1EE01431E
54. De Koninck M, Poirier S-C, Marsan B (2007) Cu x Co3 − x O4 used as bifunctional electrocatalyst: II. Electrochemical characterization for the oxygen reduction reaction. J Electrochem Soc 154(4):A381–A388

55. Lee DU, Kim BJ, Chen Z (2013) One-pot synthesis of a mesoporous $NiCo_2O_4$ nanoplatelet and graphene hybrid and its oxygen reduction and evolution activities as an efficient bi-functional electrocatalyst. J Mater Chem A 1(15):4754–4762. https://doi.org/10.1039/c3ta01402a
56. Liang Y, Wang H, Zhou J, Li Y, Wang J, Regier T, Dai H (2012) Covalent hybrid of spinel manganese–cobalt oxide and graphene as advanced oxygen reduction Electrocatalysts. J Am Chem Soc 134(7):3517–3523. https://doi.org/10.1021/ja210924t
57. Trasatti S (1980) Electrocatalysis by oxides—attempt at a unifying approach. J Electroanal Chem Interfacial Electrochem 111(1):125–131. https://doi.org/10.1016/S0022-0728(80)80084-2
58. Benhangi PH, Alfantazi A, Gyenge E (2014) Manganese dioxide-based bifunctional oxygen reduction/evolution electrocatalysts: effect of perovskite doping and potassium ion insertion. Electrochim Acta 123:42–50. https://doi.org/10.1016/j.electacta.2013.12.102
59. Kiros Y (1996) Electrocatalytic properties of Co, Pt, and Pt-Co on carbon for the reduction of oxygen in alkaline fuel cells. J Electrochem Soc 143(7):2152–2157. https://doi.org/10.1149/1.1836974
60. Qiao J, Xu L, Ding L, Shi P, Zhang L, Baker R, Zhang J (2013) Effect of KOH concentration on the oxygen reduction kinetics catalyzed by heat-treated co-pyridine/C electrocatalysts. Int J Electrochem Sci 8(1):1189–1208
61. Lucas C, Eiroa I, Nunes MR, Russo PA, Ribeiro Carrott MML, da Silva Pereira MI, Melo Jorge ME (2009) Preparation and characterization of Ca1 − x Ce x MnO3 perovskite electrodes. J Solid State Electrochem 13(6):943–950. https://doi.org/10.1007/s10008-008-0630-3
62. Du J, Zhang T, Cheng F, Chu W, Wu Z, Chen J (2014) Nonstoichiometric perovskite CaMnO3−δ for oxygen electrocatalysis with high activity. Inorg Chem 53(17):9106–9114. https://doi.org/10.1021/ic501631h
63. Messaoudi B, Joiret S, Keddam M, Takenouti H (2001) Anodic behaviour of manganese in alkaline medium. Electrochim Acta 46(16):2487–2498. https://doi.org/10.1016/S0013-4686(01)00449-2
64. Rascio DC, Souza RFBD, Teixeira Neto É, Suffredini HB, Santos MC, Calegaro ML (2010) Reaproveitamento de óxidos de manganês de pilhas descartadas para eletrocatálise da reação de redução de oxigênio em meio básico. Quím Nova 33(3):730–733. https://doi.org/10.1590/S0100-40422010000300043
65. Hamdani M, Singh R, Chartier P (2010) Co_3O_4 and Co-based spinel oxides bifunctional oxygen electrodes. Int J Electrochem Sci 5(4):556
66. Palmas S, Ferrara F, Vacca A, Mascia M, Polcaro AM (2007) Behavior of cobalt oxide electrodes during oxidative processes in alkaline medium. Electrochim Acta 53(2):400–406. https://doi.org/10.1016/j.electacta.2007.01.085
67. Palmas S, Ferrara F, Pisu A, Cannas C (2007) Oxygen evolution on Ti/Co_3O_4-coated electrodes in alkaline solution. Chem Pap 61(2):77–82
68. Lyons ME, Brandon MP (2008) The oxygen evolution reaction on passive oxide covered transition metal electrodes in aqueous alkaline solution. Part 1-Nickel. Int J Electrochem Sci 3(12):1386–1424
69. Bockris JO, Otagawa T (1983) Mechanism of oxygen evolution on perovskites. J Phys Chem 87(15):2960–2971. https://doi.org/10.1021/j100238a048
70. Hosseini-Benhangi P, Garcia-Contreras MA, Alfantazi A, Gyenge EL (2015) Method for enhancing the bifunctional activity and durability of oxygen electrodes with mixed oxide Electrocatalysts: potential driven intercalation of potassium. J Electrochem Soc 162(12):F1356–F1366. https://doi.org/10.1149/2.0561512jes
71. Sa YJ, Kwon K, Cheon JY, Kleitz F, Joo SH (2013) Ordered mesoporous Co3O4 spinels as stable, bifunctional, noble metal-free oxygen electrocatalysts. J Mater Chem A 1(34):9992–10001. https://doi.org/10.1039/c3ta11917c
72. Thangasamy P, Selvakumar K, Sathish M, Kumar SMS, Thangamuthu R (2017) Anchoring of ultrafine Co3O4 nanoparticles on MWCNTs using supercritical fluid processing and its performance evaluation towards electrocatalytic oxygen reduction reaction. Catal Sci Technol 7(5):1227–1234. https://doi.org/10.1039/C6CY02611G
73. Tulloch J, Donne SW (2009) Activity of perovskite La1−xSrxMnO3 catalysts towards oxygen reduction in alkaline electrolytes. J Power Sources 188(2):359–366. https://doi.org/10.1016/j.jpowsour.2008.12.024
74. Li X, Qu W, Zhang J, Wang H (2011) Electrocatalytic activities of La0.6Ca0.4CoO3 and La0.6Ca0.4CoO3-carbon composites toward the oxygen reduction reaction in concentrated alkaline electrolytes. J Electrochem Soc 158(5):A597–A604. https://doi.org/10.1149/1.3560170
75. Malkhandi S, Trinh P, Manohar AK, Jayachandrababu KC, Kindler A, Surya Prakash GK, Narayanan SR (2013) Electrocatalytic activity of transition metal oxide-carbon composites for oxygen reduction in alkaline batteries and fuel cells. J Electrochem Soc 160(9):F943–F952. https://doi.org/10.1149/2.109308jes
76. Mefford JT, Hardin WG, Dai S, Johnston KP, Stevenson KJ (2014) Anion charge storage through oxygen intercalation in LaMnO3 perovskite pseudocapacitor electrodes. Nat Mater 13(7):726–732. https://doi.org/10.1038/nmat4000
77. Nishio K, Molla S, Okugaki T, Nakanishi S, Nitta I, Kotani Y (2015) Oxygen reduction and evolution reactions of air electrodes using a perovskite oxide as an electrocatalyst. J Power Sources 278:645–651. https://doi.org/10.1016/j.jpowsour.2014.12.100